Imaging with Single Photon Sensitive Camera

Zhimin Wang[1,2,3]

[1]*Institute of High Energy Physics, Beijing 100049, China*
[2]*University of Chinese Academy of Sciences, Beijing 100049, China*
[3]*State Key Laboratory of Particle Detection and Electronics*

Abstract

An imaging measurement will be discussed with a single photon sensitive and low noise camera aiming to a new paradigm in the optical readout of scintillation detectors. The features of the single photon sensitive camera will be characterized and demonstrated with a measurement on double-slit Young's interference in single photon mode. This study is also trying to measure and identify muon tracks from 2D images captured by CsI(Tl) crystal scintillator detectors. The proposed approach allows for direct observation of muon tracks with a reasonable signal-to-noise ratio, eliminating the need for additional amplification or external light sources. With further enhancements to the analysis and setup, this algorithm offers an innovative method for particle measurement in low-photon environments and enables precise direction measurement of scintillation detectors.

Keywords: single photon camera, double-slit Young's interference, muon track, alpha image
DOI: 10.31526/BSM-2023.27

1. INTRODUCTION

Photon detection is one of the fundamental technologies widely used in particle physics, astronomy and industry, such as Super-K [1], KamLAND [2], JUNO [3, 4], Hubble [5], clinically and preclinically [6], X-ray imaging [7] and long-range imaging [8], etc. The reconstruction of vertex and track is critical in most of the particle physics experiments, where it is always trying to use most of information from photons. Ignoring polarization, each photon can be described by six coordinates when it is received: its impact position on the photodetector surface (x, y), the time of arrival t, two directions of propagation, θ and ϕ, and the wavelength λ [9]. Photodetectors, typically PMT or SiPM in particle physics experiments, are commonly used for light strength and timing measurements and some crude event localization. Generally, a full coverage of photodetector assemblies to the whole target guarantees an overall light collection efficiency for better precision measurement as proposed in [3].

The search for a novel technology able to detect and reconstruct events in scintillation detectors has become more and more important for dark matter and neutrino studies. An idea of detecting the light, optical and directional readout approach, proposed many years ago [10], has received renewed attention in recent years, where the challenges are the needs of high spatial resolution over large volumes, limited signal strength and non-negligible noise level [11]. The charge coupled devices (CCD) have been widely used in the past as high granularity light sensors and an upgrade of classical emulsion radiograph, such as GEM-based TPC with a 2-D CCD readout for directional dark matter experiments [12, 13, 14, 15, 16], thermal neutron imaging [17], single photon counting X-ray CCD camera spectrometer [7], photonic graph states [18], transparency measurement [19], a kilogram-scale Skipper CCD to detect coherent elastic neutrino nucleus scattering [20, 21, 22], and classical emulsion radiograph replaced by digital detector imaging especially in medicine applications [23]. At the same time, some other similar devices are also developed and used for single-photon light detection and ranging (lidar) [8, 24], and single image 3-D photography [25].

But, a critical limitation of CCD is its high level of readout noise up to one to tens electrons per pixel (RMS) comparing to the signal strength in photon counting level of particle physics experiments. Furthermore, it is commonly concluded that the scintillation detectors are fundamentally unsuitable for the imaging applications owing to the photon-starved regime and uniform angular distribution of the light produced in the scintillation process, where the limited photons emitted over a large angular range cannot be imaged through a modest aperture optical system under the limitation of the sensor noise. Homogeneous scintillation detectors give up imaging entirely, as the price to pay to collect a large fraction of the emitted photons by maximizing the coverage with low noise photon sensors, and some equal options are discussed such as "distributed imaging" with PMTs in [9].

More recently, cameras based on active pixel sensor (APS) technology developed on complementary metal-oxide semiconductors (CMOS) have been developed that can reach tens of millions of pixels with sub-electron readout noise and single photon sensitivity (usually referred as scientific CMOS (sCMOS)), where imaging, single photon imaging in particular, is providing another new possibility. It could overcome the main limitation of the CCDs on noise used for scintillation detector to offer several advantages: highly performing optical sensors can be easily procured and being developed for commercial applications; the use of suitable lenses allows the possibility of imaging large area with few sensors and better spatial resolution. A combined system of the low-noise and high-granularity cameras and fast light sensors will provide more powerful technologies and possibilities for better reconstruction of vertex and track, and benefit for a better particle identification [26]. The identification or reconstruction of particles in liquid scintillator detector also will get more possibilities by a further possible configuration (Figure 1).

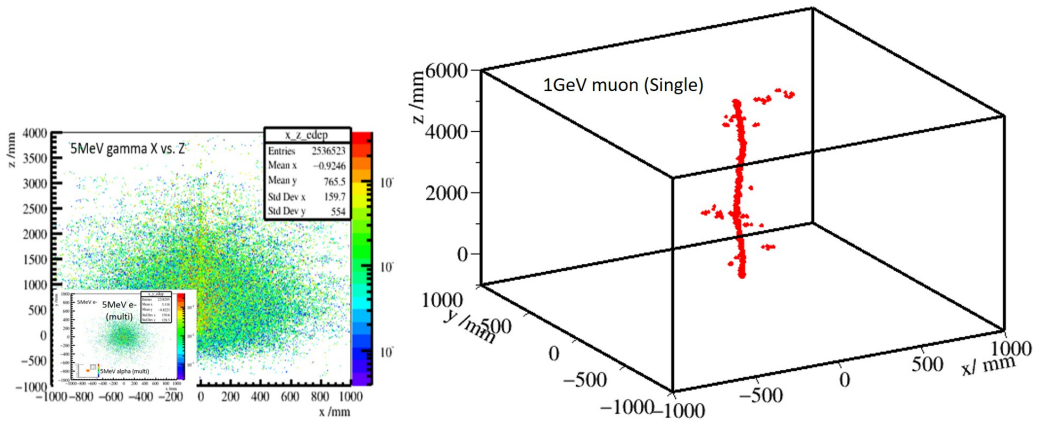

FIGURE 1: Simulated different partical response in liquid scintilator detector.

2. CHARACTERISTIC OF CAMERA

The single photon sensitive and low noise camera of ORCA-Quest qCMOS C15550-20UP is a new product of Hamamatsu Photonics [27] with a rolling shutter, 4096 (H) $\times$ 2304 (V) pixels (4.6 $\times$ 4.6 μm^2/pixel), a low-dark current to 0.006 electron/pixel/s and an ultra-low readout noise to 0.27 electron rms under ultra quiet scan. The camera can be coupled with lenses through C type interface. It will work under air cooling mode to keep the chips temperature at $-20\,^{\circ}$C here. For our study, a combined system except the camera is designed with 3-inch PMTs [28] which are working at a gain of 3×10^6 with a $\times 10$ fast amplifier to cover single photon level, and acquired by a CAEN digitizer DT5751 [29] for signal intensity monitoring in particular. The system will be re-configured manually in the following measurements including pulsed LED, crystal and double-slit Young's interference.

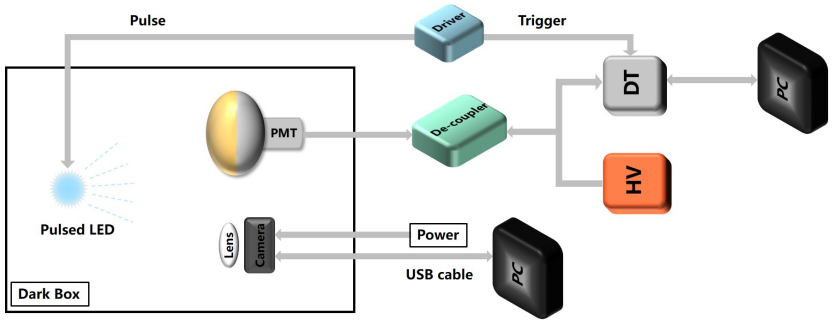

FIGURE 2: Schema of LED testing system.

Thanks to the excellent ability of the system on light intensity control and imaging, it is exciting to realize a double-slit Young's interference measurement by single photon with the re-configured system. The light intensity at the output end of the interferometer tube will be measured by the PMT, and in turn with the camera. The received light intensity on average by the PMT is set to around 0.1 photon of each pulse following Poison distribution. The camera will be run without lens to view the interference fringe directly.

The noise of the camera is measured in dark firstly, where the camera is configured in ultra-low noise mode (low frequency mode) as mentioned. Figure 3 shows the 1-D noise plot of pixels in unit of photoelectron (p.e.),[1] where the baseline is artificially shifted to 50 p.e., converted from the raw ADC by a factor of 7.8 ADC/p.e. (the baseline in ADC is at 200). The standard deviation (rms) of the distribution of all the pixels will be used to evaluate the noise level of the camera. The noise of the Hamamatsu camera is much smaller than the other two typical cameras with the same exposure time.

3. DOUBLE-SLIT YOUNG'S INTERFERENCE

As known, the wave-particle duality is one of the fundamental features of quantum mechenics, which has been measured by a lot of experiments with photons, electrons and atoms, even in single particle level [30, 31, 32, 33, 34, 35, 36, 37, 38, 39, 40, 41]. The double-slit Young's interference measurement is one of the famous experiments in the physics history and excellent interpretation

[1] Here, we will equally use the electron and photoelectron to evaluate the noise level or light intensity.

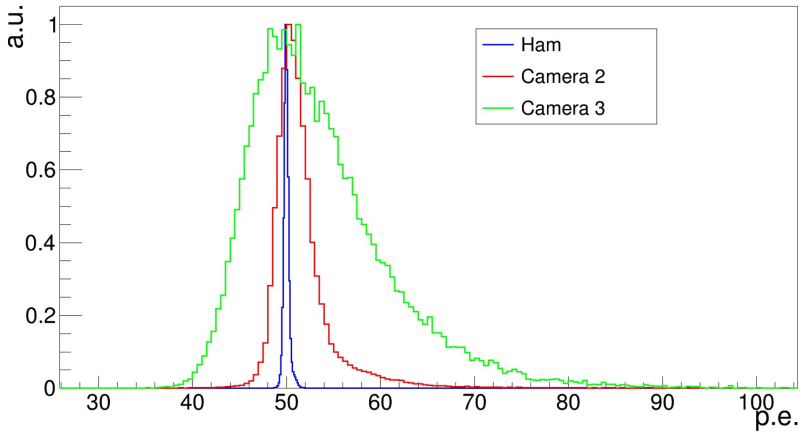

FIGURE 3: The 1-D distribution of pixel noise in p.e. of the Hamamatsu camera (blue), and other two kinds of cameras (red and green).

on quantum mechanics [42, 43, 44, 45]. While most of the previous measurements on double-slit Young's interference with single photon are configured with special light source, limited on the spatial resolution, single photon sensitivity and dynamic range of the photon sensors [41, 42, 43, 46, 47, 48]. The newly developed single-photon sensitive camera, monitored by PMT in particular, provides an excellent opportunity to realize the double-slit interference fringe in single photon level to verify the basic quantum theory directly.

With a traditional Young's double-slit interferometer, we will try to measure the interference fringe with single photon and normal LED source. The light source used here is another bare LED (3 mm, $\lambda \sim 500$ nm) without diffuser ball and working in pulse mode by a pulse driver of 100 ns width. The light intensity at the output end of the interferometer is adjusted to single photon level, which is around 0.02 p.e./pulse on average viewed by the PMT and much smaller than that. It means around 0.1 photon/pulse on average considering the QE of the PMT, where the possibility of single photon per pulse is around 0.1, and more than 2 photons per pulse is around 0.005, respectively. The relative stability of the light source monitored by PMT is around 5%. The intensities viewed by PMT with or without the slits are further measured at the output end of the interferometer: around 7.7 p.e./pulse without either slits d1 or d2, around 3.6 p.e./pulse only with slit d1 under the same LED configuration.

The interference fringe is clear when the exposure time sets to 60 s in Figure 4. The middle row of Figure 4 is showing the light intensity projected to horizontal axis of each of the interference fringe, where the intensity of the interference fringe is gradually strengthening when exposure time increasing. According to the 1-D intensity plot of all the pixels of the camera (camera noise subtracted) as shown on the bottom row of Figure 4, it is clear that most of the pixels do not receive any photons (baseline at around 200 ADC), few of the pixels receive only one photon (around 208 ADC), and the maximum is around 2 photons (around 216 ADC) with 0.1 s exposure time. Please note that, the photons can not arrive the camera at same time or single pulse duration according to the setting even single pixel can receive more than one photons. Both of the pixel number with more than 1 photons and the maximum intensity of single pixel are increasing when the exposure time increasing as expected.

4. PARTICLE IMAGING WITH CSI(TL) CRYSTAL

A $7.5 \times 7.5 \times 15\,\mathrm{cm}^3$ CsI(Tl) crystal is put in front of the camera with a distance around 10 cm (around 15 cm to the PMT). The 3-inch PMTs are used to monitor the signal intensity of the crystal, and the coincidence of the two PMTs is used as the trigger of the DT5751, where the threshold of each PMT is set to around 1 p.e.

An ^{241}Am alpha source (10 kBq, side/surface source, used for smoke alarm with a diameter of around 4 mm) is put on the top surface along horizontal direction of the crystal directly, and its rate is around 150 count per second measured by a Geiger counter near to the source surface. Here it is considered the alpha particle only (energy around 5.5 MeV), which is still the main contributor to energy deposition than the X-ray (59 keV) even considering the quenching factor [49, 50, 51].

The monitored rate is around 10 ± 1 count per second only with the crystal by the data acquisition system, and around 130 ± 10 count per second with the source with the normalization according to the selected muon rate. The PID of CsI(Tl) [52, 53] is calculated for all the events with a fast signal window of 500 ns as shown in Figure 5, where the alpha events (selected by PID > 0.45) can be identified clearly from the background, and the identified rate of muon and alpha is around 3.0 ± 0.1 Hz (by PID and total charge) and 90 ± 10 Hz at 10 cm distance, respectively. The typical intensity of single alpha event viewed by the PMT is around 80 ± 2 p.e. at 10 cm distance to the PMT. It is expected to around 8 ± 1 p.e. per alpha event viewed by the camera, which is around 1/10 to that viewed by the PMT considering the solid angle of the lens, the QE, and lens transparency.

The alpha source region is further measured with different exposure time to derive the signal strength as shown in Figure 6, where the destination region is zoomed in for detailed checking. With a taken image with exposure time 60 s, the location of the alpha source can be identified clearly as shown in the dashed red line circle. According to the zoom in of the projected plot along horizontal, the source dimension along horizontal direction is around 45 pixels, which means 3.4 mm considering the

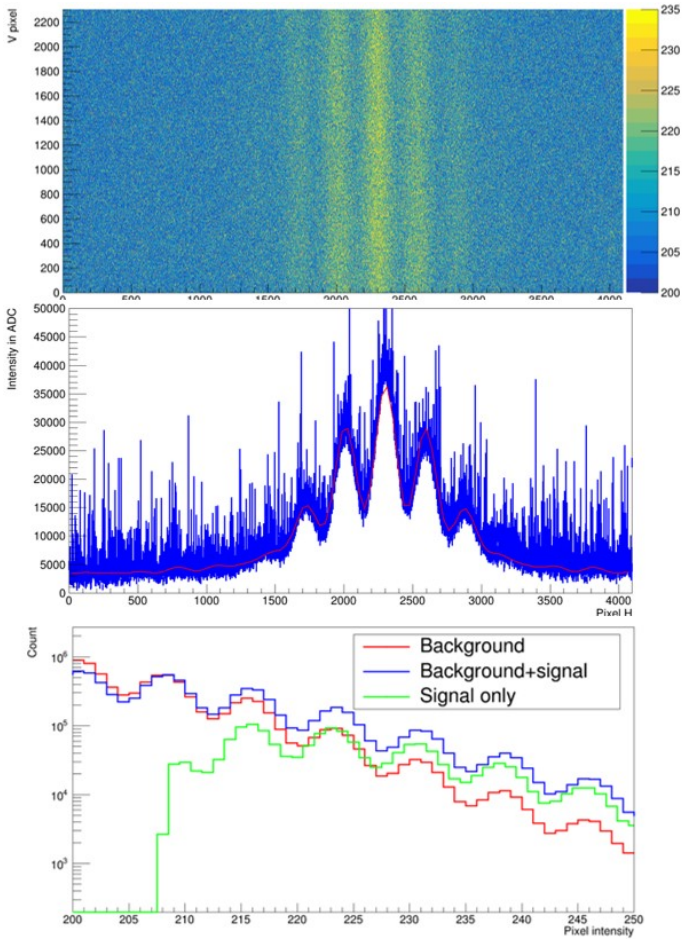

FIGURE 4: Single photon interference fringe 60 s measured by the camera with different exposure time: top row, the 2-D fringes; middle row, the 1-D intensity of fringe; bottom row, the 1-D intensity of pixels.

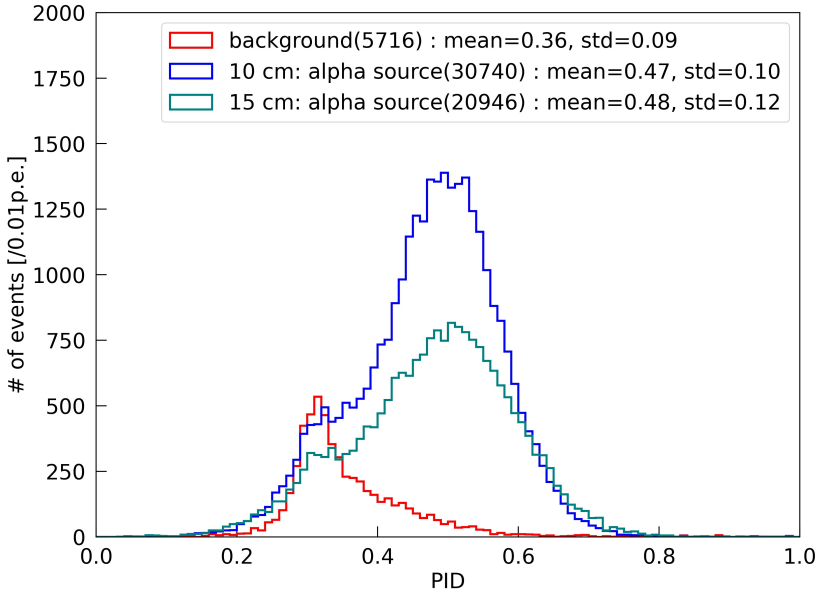

FIGURE 5: PID of crystal.

imaging magnification and basically consistent with the source dimension. According to the zoom in of the projected curve along

vertical, the energy deposit depth in vertical direction is around 15 pixels, which means around 1.1 mm considering the imaging magnification.

A radius of 22 pixels of the alpha source region (center at around pixel (2047, 1497)) is used finally to calculate the signal intensity in the following discussion. At the same time, the shape of the crystal can be identified dimly against the discrete noise because of the reflection of the crystal surface. It is clearly seen that the typical intensity of each pixel of the source region is around 260 ADC (baseline 200) or 8 p.e., and the integrated intensity of the source region on this image is around 50,000 p.e., which will be used as the measured signal strength.

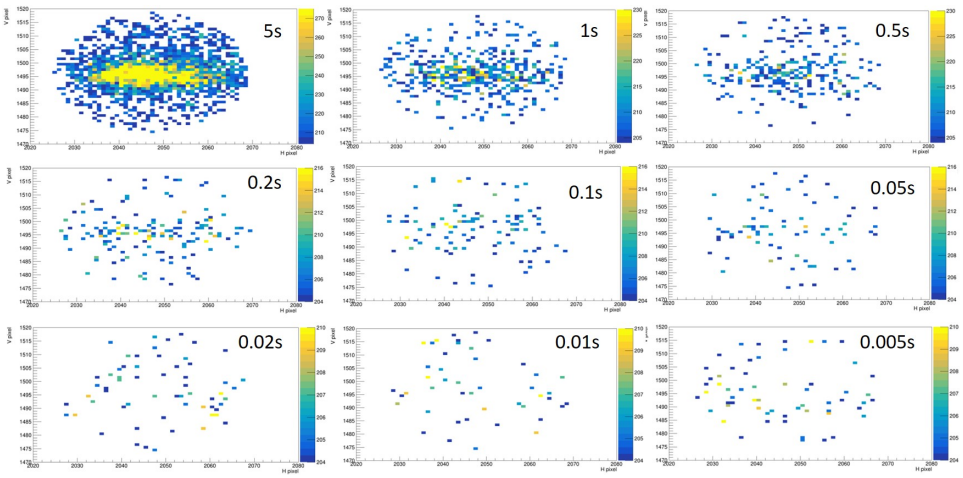

FIGURE 6: Images of crystal and alpha source with different exposure time, where the value of each pixel is in unit of ADC with 200 ADC baseline.

5. MUON TRACK & SPATIAL COINCIDENCE

It is acknowledged that the noise level of the camera used in the imaging measurements is higher compared to traditionally used PMTs or SiPMs. This becomes more challenging when employing a larger number of pixels for imaging. The signal-to-noise (S/N) ratio is proportional to the square of the reciprocal of the focal length, assuming the object distance and source intensity are fixed. This indicates that a shorter focal length can enhance the S/N ratio and improve the identification of the target, given the same object distance and source intensity.

When comparing the signal shapes of an alpha-like event in a circular area and a muon track in a straight line, it is observed that directly identifying an alpha-like event in a circular shape can be challenging due to the aimed imaging area and captured light intensity. On the other hand, a muon track is a favorable candidate for analysis if we assume its image follows a straight line with a narrow width. These results demonstrate the potential of utilizing muon tracks, which can be approximated as straight lines with a narrow width, for effective signal analysis and identification.

Images of the crystal system with the alpha source and a 1-second exposure time were captured as shown in Figure 7. The region corresponding to the source's location will serve as an online anchor for monitoring light intensity and location. Based on the calculations, the configuration with an object distance of 4 cm is continuously run with a 1-second exposure time for a total of 30 times. This is done to search for potential muon tracks that exhibit a better signal-to-noise ratio. These continuous runs and data collection aim to identify and analyze any muon tracks present in the images, allowing for a more thorough investigation of the system's performance and the detection of muon events.

Using the captured images (with an object distance of 4 cm as an example), a survey of track candidates was conducted within the target range. The target range is defined as the region between 1600 (x_1,1600) and 1700 (x_2,1700) in the vertical direction. The survey considered a minimum track length of approximately 100 pixels (vertical) and a maximum track length of around 4097 pixels (from (1, 1600) to (4096, 1700)). For each assumed line in the target range, the average pixel intensity was calculated, as depicted in Figure 8. In Figure 8, a green dotted line is plotted, representing five times the nominal noise level of the camera. This line is parameterized in the model as $(5 \times 0.3 \times 7.8\,\mathrm{ADC}/\sqrt{\text{pixel number}})$, taking into account the observed noise tails in the actual setup, as discussed in It is important to note that an offset (around 1.41 ADC) of the pixel average is related to the baseline of each pixel, which is further corrected during the sum calculation. The five-times threshold efficiently selects potential tracks while effectively rejecting noise. It is found that using a five-times threshold is more efficient than a three-times threshold, especially for track lengths shorter than 500 pixels. These findings demonstrate the effectiveness of the five-times threshold in distinguishing signal tracks from noise, particularly for shorter track lengths.

It is noted that the observed number of track candidates is several tens per second, which is higher than the expected rate of three muons per second hitting the crystals. Furthermore, some of the candidate tracks exhibit directions and locations that exceed the range of the lens's field of view. This suggests the possibility of additional sources or artifacts contributing to the observed

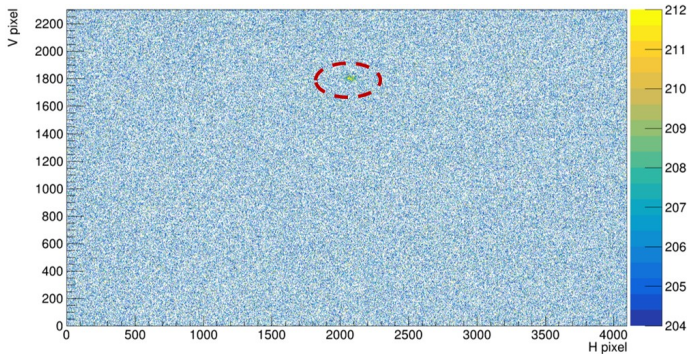

FIGURE 7: Full image of the crystal with alpha source under 1 s exposure time: object distance of 4 cm.

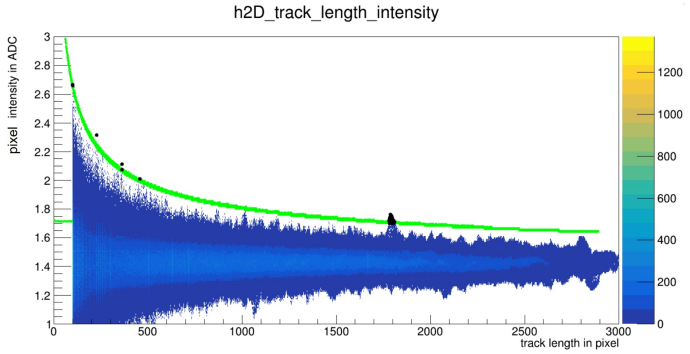

FIGURE 8: Average pixel intensity versus track length.

tracks. Additionally, there are instances where multiple track candidates are located near each other (indicated by yellow lines in Figure 9). These close proximity track candidates could be attributed to potential tracks or correlated noise within the system. It is important to note that further investigations and checks are necessary to verify the quality and origin of these track identifications. These checks will help determine whether the identified candidates are indeed muon tracks or if they are influenced by other factors such as noise or system artifacts.

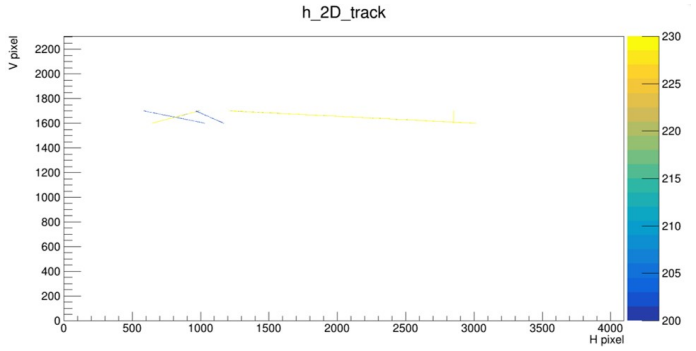

FIGURE 9: Selected candidates of tracks under 1 s exposure time. The z-axis is the measured value in ADC of each pixel.

To further verify the identified track candidates as potential muon tracks, a check is performed by extending each track along its candidate direction. The extension is done by adding an additional 2000 pixels or extending up to the edge of the photo. This extension allows for an examination of the summed intensity along the track. Upon inspection, it is observed that most of the candidates are excluded after the extension, as they fail to meet the requirement of having an average pixel intensity larger than five times the noise level. Additionally, the sum of pixel intensities along the track for a few candidates continues to increase as the track length extends, which is expected for true muon tracks. Moreover, the average pixel intensity for these candidates exceeds the five-times threshold. These findings suggest that most of the candidates can be excluded as potential muon tracks, while a few candidates exhibit characteristics consistent with true muon tracks. However, it is important to note that further checks and analysis are necessary to confirm the quality and authenticity of these identified candidates.

The intensity distribution is displayed in Figure 10. The raw length of this candidate is approximately 1786 pixels (which extends to around 2880 pixels after the track extension). The averaged intensity per pixel is around 0.318 ADC (after subtracting

the baseline offset of 1.41 ADC from the raw value of 1.728 ADC). The summed intensity along the track is approximately 568 ADC over 1786 pixels, equivalent to around 73 photoelectrons (p.e.). Considering the expected spread of muon charge intensity, both of these candidates demonstrate characteristics that make them potentially good candidates for muon tracks. However, it is crucial to conduct further analysis and verification to confirm their nature as genuine muon tracks. Furthermore, a measurement with possible spatial coincidence is very useful to suppress the noise of camera as shown in Figure 11.

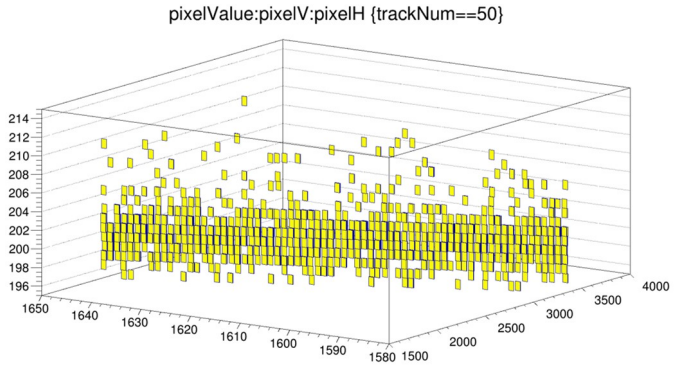

FIGURE 10: Extended track in 3D.

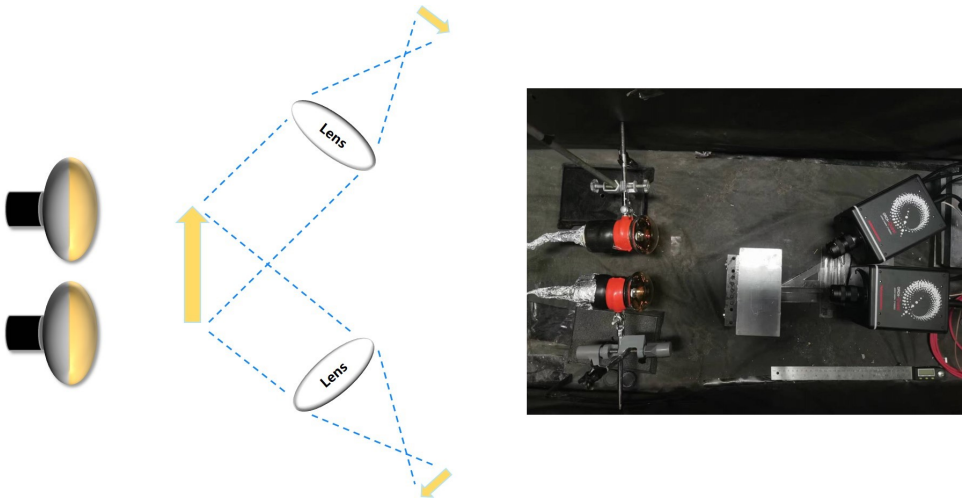

FIGURE 11: Spatial coincidence.

6. SUMMARY

The single photon sensitive and low noise camera provides another novel possibility for imaging for the photon-starved regime and uniform angular distribution of scintillation detectors. With a combined system constituted by 3-inch PMTs and the camera, the double-slit Young's interference with a single photon can be achieved, and a single ^{241}Am alpha event with CsI(Tl) crystal is closely to be distinguished. A spatial coincidence system is further proposed as an attractive option to suppress the random noise of the camera and improve the signal-to-noise ratio, where the lenses with a larger effective aperture are also favored for further applications. The imaging of muon tracks was further tested, and the data were analyzed based on the expected characteristics. Some potential tracks were identified using averaged signal intensity cuts. However, there are still a few crucial aspects that need to be finalized, and several improvements have been proposed and suggested. The achievement of direct measurement of muon tracks holds significant value for future experiments and applications. With further advancements and improvements, the realization of direct measurement of muon tracks through the proposed system is a valuable advancement with potential applications in various fields.

ACKNOWLEDGMENTS

This work was supported by the National Natural Science Foundation of China No. 11875282, the State Key Laboratory of Particle Detection and Electronics, SKLPDE-ZZ-202208. The author would like to thank Mr. Mengyun Guan for the valuable discussions.

References

[1] S. Fukuda et al. The super-kamiokande detector. *Nuclear Instruments and Methods in Physics Research Section A: Accelerators, Spectrometers, Detectors and Associated Equipment*, 501(2):418–462, 2003.
[2] K. Eguchi et al. First results from kamland: Evidence for reactor antineutrino disappearance. *Phys. Rev. Lett.*, 90:021802, Jan 2003.
[3] JUNO Collaboration. Juno physics and detector. *Progress in Particle and Nuclear Physics*, 123:103927, 2022.
[4] Angel Abusleme et al. Mass testing and characterization of 20-inch pmts for JUNO. In *arXiv e-prints*, 2022. arXiv:2205.08629.
[5] Holland C. Ford et al. Advanced camera for the Hubble Space Telescope. In Pierre Y. Bely and James B. Breckinridge, editors, *Space Telescopes and Instruments V*, volume 3356, pages 234–248. International Society for Optics and Photonics, SPIE, 1998.
[6] Pat Zanzonico. *Instrumentation for Single-Photon Emission Imaging*, pages 1–23. Springer International Publishing, Cham, 2016.
[7] Nandan Jha et al. Single photon counting X-ray CCD camera spectrometer. In *Conference: NLS-22 (National Laser symposium-22)*, 01 2014.
[8] Zheng-Ping Li et al. Single-photon computational 3D imaging at 45 km. *Photon. Res.*, 8(9):1532–1540, Sep 2020.
[9] J. Dalmasson et al. Distributed imaging for liquid scintillation detectors. *Phys. Rev. D*, 97:052006, Mar 2018.
[10] W. Dominik et al. A gaseous detector for high-accuracy autoradiography of radioactive compounds with optical readout of avalanche positions. *Nuclear Instruments and Methods in Physics Research Section A: Accelerators, Spectrometers, Detectors and Associated Equipment*, 278(3):779–787, 1989.
[11] J. B. R. Battat et al. Readout technologies for directional wimp dark matter detection. *Physics Reports*, 662:1–46, 2016. Readout technologies for directional WIMP Dark Matter detection.
[12] N. S. Phan, R. J. Lauer, E. R. Lee, D. Loomba, J. A. J. Matthews, and E. H. Miller. Gem-based tpc with ccd imaging for directional dark matter detection. *Astroparticle Physics*, 84:82–96, 2016.
[13] Alexander Deisting et al. Commissioning of a high pressure time projection chamber with optical readout. *Instruments*, 5(2), 2021.
[14] N. S. Phan, E. R. Lee, and D. Loomba. Imaging 55fe electron tracks in a GEM-based TPC using a CCD readout. *Journal of Instrumentation*, 15(05):P05012–P05012, may 2020.
[15] F. A. F. Fraga et al. CCD readout of gem-based neutron detectors. *Nuclear Instruments and Methods in Physics Research Section A: Accelerators, Spectrometers, Detectors and Associated Equipment*, 478(1):357–361, 2002. Proceedings of the ninth Int.Conf. on Instrumentation.
[16] K. Mavrokoridis et al. Optical readout of a two phase liquid argon tpc using ccd camera and thgems. *Journal of Instrumentation*, 9, 01 2014.
[17] Ilan Mor, Nissan Eldad, Moshe Cohen, and Reuven Hacham-Zada. Development of a ccd based thermal neutron imaging detector for the israeli research reactor irr-1 at soreq nrc. *Nuclear Instruments and Methods in Physics Research Section A: Accelerators, Spectrometers, Detectors and Associated Equipment*, 1012:165632, 2021.
[18] Jin-Peng Li et al. Multiphoton graph states from a solid-state single-photon source. *ACS Photonics*, XXXX, 06 2020.
[19] Zhangquan Xie et al. A liquid scintillator for a neutrino detector working at -50 degree. *Nuclear Instruments and Methods in Physics Research Section A: Accelerators, Spectrometers, Detectors and Associated Equipment*, 1009:165459, 2021.
[20] Guillermo Fernandez-Moroni et al. The physics potential of a reactor neutrino experiment with skipper ccds: measuring the weak mixing angle. *Journal of High Energy Physics*, 2021, 03 2021.
[21] Alexis Aguilar-Arevalo et al. Reactor neutrino detection experiment using skipper ccds, 2020.
[22] Fernandez Moroni et al. Charge coupled devices for detection of coherent neutrino-nucleus scattering. *Phys. Rev. D*, 91:072001, Apr 2015.
[23] David Schumacher, Uwe Zscherpel, and Uwe Ewert. Photon counting and energy discriminating X-ray detectors - benefits and applications. In *19th World Conference on Non-Destructive Testing*, 2016.
[24] Micro Photon Devices S.r.l. Spc: Single photon counting camera, 2018.
[25] Varun Jampani et al. SLIDE: Single image 3D photography with soft layering and depth-aware inpainting. *e-print*, 2021.
[26] Fernando Domingues Amaro et al. The cygno experiment. *Instruments*, 6(1), 2022.
[27] Hamamatsu Photonics. ORCA-Quest qCMOS camera C15550-20UP, 2021. https://www.hamamatsu.com/jp/en/product/cameras/qcmos-cameras/C15550-20UP.html.
[28] Chuanya Cao et al. Mass production and characterization of 3-inch pmts for the juno experiment. *Nuclear Instruments and Methods in Physics Research Section A: Accelerators, Spectrometers, Detectors and Associated Equipment*, 1005:165347, 2021.
[29] C.A.E.N. DT5751 2/4 Channel 10 bit 2/1 GS/s Digitizer, 2015. https://www.caen.it/products/dt5751/.
[30] L. Marton, J. Arol Simpson, and J. A. Suddeth. An electron interferometer. *Review of Scientific Instruments*, 25(11):1099–1104, 1954.
[31] Giorgio Matteucci, Michele Pezzi, Giulio Pozzi, Gian Luigi Alberghi, Filippo Giorgi, Alessandro Gabrielli, Nicola Semprini Cesari, Mauro Villa, Antonio Zoccoli, Stefano Frabboni, and Gian Carlo Gazzadi. Build-up of interference patterns with single electrons. *European Journal of Physics*, 34(3):511–517, Mar 2013.
[32] John C. H. Spence. *Electron Interferometry*, pages 188–195. Springer Berlin Heidelberg, Berlin, Heidelberg, 2009.
[33] L. Marton, J. Arol Simpson, and J. A. Suddeth. Electron beam interferometer. *Phys. Rev.*, 90:490–491, May 1953.
[34] Francis M. Pipkin. *Atomic Physics Tests of the Basic Concepts in Quantum Mechanics**The preparation of this manuscript was supported in part by the Department of Energy and the National Science Foundation.*, volume 14 of *Advances in Atomic and Molecular Physics*, pages 281–340. Academic Press, 1979.
[35] P. Grangier, G. Roger, and A. Aspect. Experimental evidence for a photon anticorrelation effect on a beam splitter: A new light on single-photon interferences. *Europhysics Letters (EPL)*, 1(4):173–179, Feb 1986.
[36] A. Tonomura et al. Demonstration of single-electron buildup of an interference pattern. *American Journal of Physics*, 57:117, 1989.
[37] Herbert Walther Marian O. Scully, Berthold-Georg Englert. Quantum optical tests of complementarity. *Nature*, 351:111–116, May 1991.
[38] L. Mandel. Quantum effects in one-photon and two-photon interference. *Rev. Mod. Phys.*, 71:S274–S282, Mar 1999.
[39] Roger Bach, Damian Pope, Sy-Hwang Liou, and Herman Batelaan. Controlled double-slit electron diffraction. *New Journal of Physics*, 15(3):033018, Mar 2013.
[40] Ángel S. Sanz and Salvador Miret-Artés. *Quantum Interference and Superposition*, pages 49–95. Springer Berlin Heidelberg, Berlin, Heidelberg, 2014.
[41] Sacha Kocsis, Boris Braverman, Sylvain Ravets, Martin J. Stevens, Richard P. Mirin, L. Krister Shalm, and Aephraim M. Steinberg. Observing the average trajectories of single photons in a two-slit interferometer. *Science*, 332(6034):1170–1173, 2011.
[42] Physics World. The double-slit experiment. *Physics World*, 15(9):15–15, Sep 2002.
[43] James Q. Quach. Which-way double-slit experiments and born-rule violation. *Phys. Rev. A*, 95:042129, Apr 2017.
[44] Feynman R. P., Leighton R. B., Sands M. *The Feynman Lectures on Physics*. Addison-Wesley Publishing Company, 3rd edition, 1963.
[45] A. H. Tavabi et al. The young-feynman controlled double-slit electron interference experiment. *Sci Rep*, 9(10458), 2019.
[46] Hans De Raedt, Kristel Michielsen, and Karl Hess. Analysis of multipath interference in three-slit experiments. *Phys. Rev. A*, 85:012101, Jan 2012.

[47] Urbasi Sinha, Christophe Couteau, Thomas Jennewein, Raymond Laflamme, and Gregor Weihs. Ruling out multi-order interference in quantum mechanics. *Science*, 329(5990):418–421, 2010.
[48] Omar S. Magaña-Loaiza et al. Exotic looped trajectories of photons in three-slit interference. *Nature Communications*, 7:13987, 12 2016.
[49] H. Park et al. Neutron beam test of csi crystal for dark matter search. *Nuclear Instruments and Methods in Physics Research Section A: Accelerators, Spectrometers, Detectors and Associated Equipment*, 491(3):460–469, 2002.
[50] C. Guo et al. Neutron beam tests of csi(na) and caf2(eu) crystals for dark matter direct search. *Nuclear Instruments and Methods in Physics Research Section A: Accelerators, Spectrometers, Detectors and Associated Equipment*, 818:38–44, 2016.
[51] J. H. Lee et al. Measurement of the quenching and channeling effects in a csi crystal used for a wimp search. *Nuclear Instruments and Methods in Physics Research Section A: Accelerators, Spectrometers, Detectors and Associated Equipment*, 782:133–142, 2015.
[52] F. Benrachi, B. Chambon, B. Cheynis, D. Drain, C. Pastor, D. Seghier, K. Zaid, A. Giorni, D. Heuer, A. Llères, C. Morand, P. Stassi, and J. B. Viano. Investigation of the performance of csi(tl) for charged particle identification by pulse-shape analysis. *Nuclear Instruments and Methods in Physics Research Section A: Accelerators, Spectrometers, Detectors and Associated Equipment*, 281(1):137–142, 1989.
[53] T. Teranishi, Y. Ueno, M. Osada, S. Oka, K. Iribe, H. Yoshida, H. Sakai, and T. Kubo. Pulse shape analysis of signals from sipm-based csi(tl) detectors for low-energy protons: Saturation correction and particle identification. *Nuclear Instruments and Methods in Physics Research Section A: Accelerators, Spectrometers, Detectors and Associated Equipment*, 989:164967, 2021.